LIMNOLOGY and OCEANOGRAPHY: METHODS

ASLO

Limnol. Oceanogr.: Methods 2023

doi: 10.1002/lom3.10572

A novel fluoro-electrochemical technique for classifying diverse marine nanophytoplankton

Samuel Barton,[1]* **Minjun Yang**,[2] **Haotian Chen**,[2] **Christopher Batchelor-McAuley**,[2,3] **Richard G. Compton**,[2] **Heather A. Bouman**,[1] **Rosalind E. M. Rickaby**[1]

[1]Department of Earth Sciences, University of Oxford, Oxford, UK
[2]Physical and Theoretical Chemistry Laboratory, Department of Chemistry, University of Oxford, Oxford, UK
[3]School of Chemistry, Trinity College Dublin, Dublin 2, Ireland

Abstract

To broaden our understanding of pelagic ecosystem responses to environmental change, it is essential that we improve the spatiotemporal resolution of in situ monitoring of phytoplankton communities. A key challenge for existing methods is in classifying and quantifying cells within the nanophytoplankton size range (2–20 μm). This is particularly difficult when there are similarities in morphology, making visual differentiation difficult for both trained taxonomists and machine learning-based approaches. Here we present a rapid fluoro-electrochemical technique for classifying nanophytoplankton, and using a library of 52 diverse strains of nanophytoplankton we assess the accuracy of this technique based on two measurements at the individual level: charge required to reduce per cell chlorophyll *a* fluorescence by 50% and cell radius. We demonstrate a high degree of accuracy overall (92%) in categorizing cells belonging to widely recognized key functional groups; however, this is reduced when we consider the broader diversity of "nano-phytoflagellates'." Notably, we observe that some groups, for example, calcifying Isochrysidales, have much greater resilience to electrochemically driven oxidative conditions relative to others of a similar size, making them more easily categorized by the technique. The findings of this study present a promising step forward in advancing our toolkit for monitoring phytoplankton communities. We highlight that, for improved categorization accuracy, future iterations of the method can be enhanced by measuring additional predictor variables with minimal adjustments to the set-up. In doing so, we foresee this technique being highly applicable, and potentially invaluable, for in situ classification and enumeration of the nanophytoplankton size fraction.

The essential role that phytoplankton play in sustaining marine ecosystems and driving key biogeochemical cycles, notably the biological carbon pump, is unequivocal. As we progress through the Anthropocene, the oceans are facing unprecedented rates of environmental change. In order to improve our global understanding of the impacts that such change is having on phytoplankton communities, and how this might impact key ecosystems services, we must advance our ability to monitor phytoplankton community structure, both spatially and temporally. It is pertinent that in situ measurements can capture and quantify the abundance of dominant functional groups of phytoplankton that are present (i.e., groups with different biogeochemical and/or ecological functions), as this can inform us about the likely implications of environmental change for marine food webs, biogeochemical cycles, and the capacity of such communities to contribute to sequestration of dissolved CO_2. Widely recognized functional groups include (but are not limited to): coccolithophores, diatoms, dinoflagellates, and cyanobacteria (Anderson 2005; Nair et al. 2008; Anderson et al. 2021).

An important consideration when attempting to quantitatively assess in situ phytoplankton communities is that, as single unicellular organisms, phytoplankton can exhibit a large variation in size, spanning over four orders of magnitude;

*Correspondence: samuel.barton@earth.ox.ac.uk

Author Contribution Statement: S.B., M.Y., C.B.-M., R.G.C., H.A.B., and R.E.M.R. conceptualized the study. S.B. (phytoplankton), M.Y., and C.B.-M (electrochemistry) contributed to the methodology. S.B. conducted the experiments. S.B. and M.Y. analyzed the data. S.B. wrote the manuscript. M.Y., H.C., C.B.-M., R.G.C., H.A.B., and R.E.M.R., reviewed and edited the manuscript.

Additional Supporting Information may be found in the online version of this article.

ranging in length from picophytoplankton < 2 μm (including most cyanobacteria and picoeukaryotes) to the largest diatoms > 1000 μm (Snoeijs et al. 2002; Finkel et al. 2010). From an ecological perspective, size is considered a master trait and is known to significantly influence growth rates, nutrient requirements, grazing susceptibility, and sinking rates (Litchman and Klausmeier 2008); all of which have a bearing on important biogeochemical cycles. In this respect, it has been demonstrated that eukaryotic unicells in the nanophytoplankton size range (2–20 μm) display the greatest mass-specific metabolic rates, and thus growth rates, relative to larger microphytoplankton (20–2000 μm) and smaller picophytoplankton (Marañón et al. 2013; López-Sandoval et al. 2014; Ward et al. 2017), making them highly competitive and fast responding to environmental perturbations. Indeed, the general success of nanophytoplankton and their ability to dominate phytoplankton biomass has been widely demonstrated from field-based measurements in both the open-ocean (Tarran et al. 2006; Balzano et al. 2012; de Vargas et al. 2015; Bolaños et al. 2020) and coastal waters (Barnes et al. 2015; Pinckney et al. 2015; Alves-De-Souza et al. 2017; Leblanc et al. 2018; Piwosz 2019). Subsequently, as sentinels of the phytoplankton assemblage, nanophytoplankton are an insightful target area for monitoring phytoplankton ecological and biogeochemical functioning in response to ocean change. To date, however, there are numerous constraints and limitations to the available methods in obtaining in situ time series measurements of nanophytoplankton diversity and abundance.

Arguably, the most accurate method for quantifying phytoplankton abundance is microscope taxonomy. If specifically focusing on the nanophytoplankton size fraction, taxonomists can quantify abundance to the genus and species level when there are easily identifiable cell characteristics or morphologies (e.g., the unique extracellular calcite structures of coccolithophores, or the complex silica frustules of diatoms). However, this size fraction also contains a large proportion of cell types (typically between 2 and 10 μm) that are extremely hard to identify due to their similar morphology and lack of external inorganic structure (Widdicombe et al. 2010; Piwosz 2019). As a result, a significant proportion of the nanophytoplankton fraction is often given the blanket label of "nano-phytoflagellates" (or similar) in taxonomy surveys. For example, a long-term time series (> 15 years) of the pelagic phytoplankton communities at the L4 station in the Western English Channel has consistently observed that these "nano-phytoflagellates" make up > 80% of the total cell counts per unit volume (Widdicombe et al. 2010). The other main limitations of traditional microscopy are that it is time-consuming in nature, requires highly skilled labor input, and live samples being fixed and preserved prior to analysis.

Flow cytometry is a higher throughput quantitative approach that is often used to distinguish nanophytoplankton and picophytoplankton size fractions, of either live or fixed samples. Light scattering and autofluorescence detection allow for clustering of cells with similar optical properties. This gives a high degree of separation within the picophytoplankton size fraction, as the cyanobacteria autofluorescence and scattering signal is distinct from that of picoeukaryotes (Collier 2000). Where cytometry falls short is at being able to fully characterize ecologically relevant components of the nanophytoplankton fraction; only coccolithophores (detectable due to their unique light scattering) and cryptophytes (due to their phycoerythrin content) can be discriminated from other nanoeukaryotes (Tarran et al. 2006; Tarran and Bruun 2015). Thus, in order to obtain a true representation of the species present in the nanophytoplankton fraction, previous studies have often complemented microscope taxonomy and cytometry analyses with genetics-based interpretations (Balzano et al. 2012; Leblanc et al. 2018; Piwosz 2019; Bolaños et al. 2020; Stern et al. 2023), which generally only provide a value for relative abundances.

Over the last decade or so, there has been an increased application of rapid throughput imaging flow cytometry (Lombard et al. 2019). This technique demonstrates a high degree of accuracy in classifying phytoplankton cell types from a combination of image-based machine learning and autofluorescence measurements (Olson and Sosik 2007; Sosik and Olson 2007; Álvarez et al. 2014; Dugenne et al. 2014; Camoying and Yñiguez 2016; Fragoso et al. 2019; Fuchs et al. 2022; Irisson et al. 2022; Kraft et al. 2022); thereby, in essence, merging the identification skills of a microscope taxonomist, with the speed and tools of a flow cytometer. The FlowCam (Yokogawa Fluid Imaging Technologies, Inc.) is a laboratory-based device (Sieracki et al. 1998) that has been shown to produce highly comparable results when validated alongside traditional microscopical estimates (Álvarez et al. 2014) and, depending upon the FlowCam model, can analyze a broad range of particle sizes from 300 nm to 1 mm. As with microscope techniques, however, the current models of FlowCam still struggle to classify nanophytoplankton cells that have similar sizes and morphologies. Like FlowCam, the CytoSense (CytoBuoy b.v.) is a non-submersible imaging flow cytometry device that has also performed well alongside traditional microscope taxonomy, but validation is poor for classifying cells that are < 5 μm in size (Haraguchi et al. 2017). The Imaging FlowCytobot, or IFCB (McClane Research Laboratories, Inc), and CytoBuoy (CytoBuoy b.v.) are devices that operate similarly to those above, but have been developed to function autonomously at sea (Dubelaar et al. 1999; Olson and Sosik 2007; Fragoso et al. 2019). These are promising steps forward for the generation of in situ spatio-temporal data for monitoring phytoplankton community structure. Indeed, a recent study has shown strong correlation between IFCB measurements and microscopy data for quantifying blooms of filamentous cyanobacteria in the Baltic Sea (Kraft et al. 2021). Nonetheless, while the imaging of these devices covers a broad

size range, with the IFCB imaging between 10 and 150 μm and the CytoBuoy from 1 to 778 μm, both devices are reported to have poor resolution at their lower detection limits necessary for categorizing and quantifying nanophytoplankton (Dugenne et al. 2014; Fragoso et al. 2019; Bolaños et al. 2020; Chase et al. 2020; Fuchs et al. 2022). Furthermore, despite advancements in the machine learning techniques used to improve the classification of data obtained from such devices (Fuchs et al. 2022; Kraft et al. 2022), this is only as good as the resolution of the images acquired and the human interpretation that drives the training (Irisson et al. 2022). This presents a substantial challenge in the nanophytoplankton size range, where there are constraints on image resolution at the finer scale (dependent on the objective lens and camera technology employed), along with human limitations in validating (not all nanophytoplankton are easily distinguishable due to similar size and morphology). We therefore identify that a key frontier in monitoring the health of pelagic ecosystems is in developing novel high-throughput techniques that allow for higher resolution in situ discrimination and quantification in the nanophytoplankton size range.

Moving forward, recent developments in the field of analytical chemistry have shown that electrochemically induced oxidative stress destroys phytoplankton chlorophyll *a* (Chl *a*) fluorescence in a manner that is idiosyncratic, allowing for differentiation of phytoplankton species from measurements that are obtained within 10s of seconds (Yang et al. 2019; Yu et al. 2022). When a sufficiently high potential is applied to an electrode that is immersed in seawater, a wide range of oxidants can form and diffuse from the electrode surface, for example; oxidation of water to hydrogen peroxide and hydroxyl radicals, bromide to hypobromous acid, and chloride to dichlorine (Yang et al. 2019; Yu et al. 2022). The subsequent reaction of these oxidants with phytoplankton is seen to cause a rapid decay of the cellular Chl *a* fluorescence signal. The rate at which this happens is dependent on a number of factors, including; the distance of the phytoplankton cells from the electrode, the potential applied (and thus the species and concentration of oxidants generated), and more importantly for the work presented here—the type of phytoplankton cell. To that end, we apply this novel fluoro-electrochemical method to a much broader suite of ecologically relevant picophytoplankton and nanophytoplankton (52 cultured strains) to produce a "susceptibility library" based on two variables; Chl *a* fluorescence "switch-off" and measured cell radius. This library is assessed using a random forest approach to determine how well the electrochemical method can be used to classify cells into relevant groups. We specifically focused on strains of nanophytoplankton that (a) represent key functional groups and (b) represent some of the traditionally hard to identify "nano-phytoflagellates." We then explore a possible biological underpinning to the method, as well as discussing its current limitations and suggested improvements.

Methods and procedures

Culturing for the "susceptibility library"

Phytoplankton monocultures were selected so that we had a good representation of each of the key functional groups (5 groups, represented by 37 strains in total), along with an assortment of strains that we consider to be likely "nano-phytoflagellate" candidates (6 groups, represented by 15 strains in total, within the 2–10 μm size range). The key functional groups that we analyze are herein labeled as: "Calcifying Isochrysidales" (7 strains), "Coccolithophores" (8 strains), "Diatoms" (10 strains), "Dinoflagellates" (8 strains), and "Picophytoplankton" (4 strains). In this instance, "Calcifying Isochrysidales" includes strains of both *Emiliania huxleyi* (6 strains) and *Gephyrocapsa oceanica* (1 strain). Although they might both be considered coccolithophores, given their cosmopolitan nature and the fact they are the most globally abundant calcifiers (particularly *E. huxleyi*) we considered them as a separate group for this analysis. We also chose to include a range of *E. huxleyi* cell stages (both calcified and non-calcified diploid strains, along with a haploid strain) and morphologies (representing different extents of calcification), allowing us to robustly investigate the within species variance in the electrochemical susceptibility. Picophytoplankton are included to allow us to test the lower size limits for detection and classification of our method, including two strains of cyanobacteria (both *Synechococcus* sp.) and two pico-eukaryotes (*Micromonas pusilla* and *Ostreococcus tauri*). Broadening the dataset to encompass nanophytoplankton beyond the key functional groups, the additional groups in our analysis were as follows: "Eustigmatales" (1 strain), "Green algae" (3 strains), "Non-calcifying Isochrysidales" (4 strains), "Pavlovales" (3 strains), "Phaeocystales" (1 strain), and Prymnesiales (3 strains). These strains were selected as it has previously been noted that the unrecognizable "nano-phytoflagelletes," which are a challenge for microscope taxonomy, could broadly be assigned to the phyla of haptophytes (non-calcified types), chlorophytes (or green algae), and cryptophytes (Piwosz 2019). A full list of the 52 strains used in this study can be found in Supporting Information Table S1. In the case of "Eustigmatales" we assume that a single strain of *Nannochloropsis granulata* is broadly representative, and for "Phyaeocystales" we worked with a single strain of *Phaeocystis globosa*.

All strains were obtained from reputable culture collections: Roscoff Culture Collection (Roscoff, France), Culture Collection of Algae and Protozoa (Oban, UK) and The Marine Biological Association (Plymouth, UK). Following their arrival, they were maintained in exponential growth through regular subculturing under sterile conditions on their advised growth medium (*see* Supporting Information Table S1). All growth media were prepared using synthetic ocean water (Morel et al. 1979), allowing greater control over the main composition of the seawater (*see* Supporting Information Table S2), and thus consistency in the probable oxidants formed when

measuring the electrochemical responses (note that a negligible effect of growth medium on the susceptibility to the electrochemical stress was observed when compared alongside natural seawater; *see* Supporting Information Fig. S3). Cultures were incubated in PHCbi MLR-352-PE Incubators (PHC Europe B.V.) set to 17°C (or 20°C for all diatoms), with a 14 : 10 h light–dark regime at a photosynthetically active radiation (PAR) intensity of 20–40 μmol m^{-2} s^{-1}, and were kept under these conditions for a minimum of 2 months prior to carrying out the electrochemical susceptibility measurements. The growth of the cultures was tracked on a daily basis using a TECAN Spark plate reader (Tecan Group Ltd.), where three technical replicates of 200 μL of each culture were measured for Chl *a* fluorescence as a proxy for culture biomass. We then selected a time-point in mid-exponential growth phase, when each strain was not at saturation point (i.e., carrying capacity) and therefore not nutrient limited, to conduct our experiments (*see* Supporting Information Fig. S1); however, for a couple of strains, susceptibility measurements were taken at different growth phases (and thus different nutrient availability) and only a minimal difference was observed across the phases (*see* Supporting Information Fig. S4). Immediately prior to the electrochemical experiments, to obtain a sufficient number of cells per image series (as described below), all strains were concentrated by centrifugation (Centrifuge 5702, Eppendorf UK Limited) at 1000 r.p.m for 10 min, and resuspended to a concentration typically ranging between 5× and 10×.

The fluoro-electrochemical technique

A more detailed description of the fundamental electrochemical principles and details of the underlying methodology, including specifics of the equipment used, can be found in the previously published work by Yu et al. (2022). For the purposes of this study, the step-by-step method described below outlines the essential procedures that were followed to yield the underlying dataset for the susceptibility library. In summary, we used a galvanostat-based ramping linear current, applied to phytoplankton cells settled onto the surface of a carbon electrode (thus controlling for distance from the electrode) and monitored Chl *a* fluorescence decay over time per individual cell (*see* Supporting Information Table S3 for number of individual cell measurements per strain). The constant rate of current ramping (10 μA s^{-1}) means that the moles of oxidant being generated electrochemically increases with time in a controlled fashion. This approach allows for greater possible discrimination of phytoplankton cell types and over a shorter experimental time frame (e.g., 10s of seconds), as opposed to running experiments at a single set potential. Consequently, as cell types have different levels of resilience to such oxidative stress, this technique enables us to quantify the differences in time that is required to drive the Chl *a* quenching across the phytoplankton investigated.

The fluoro-electrochemical measurements were made as follows (*see* Fig. 1a, adapted from Yu et al. 2022):

1. A concentrated sample from a phytoplankton monoculture in exponential growth phase (as described in the Culturing

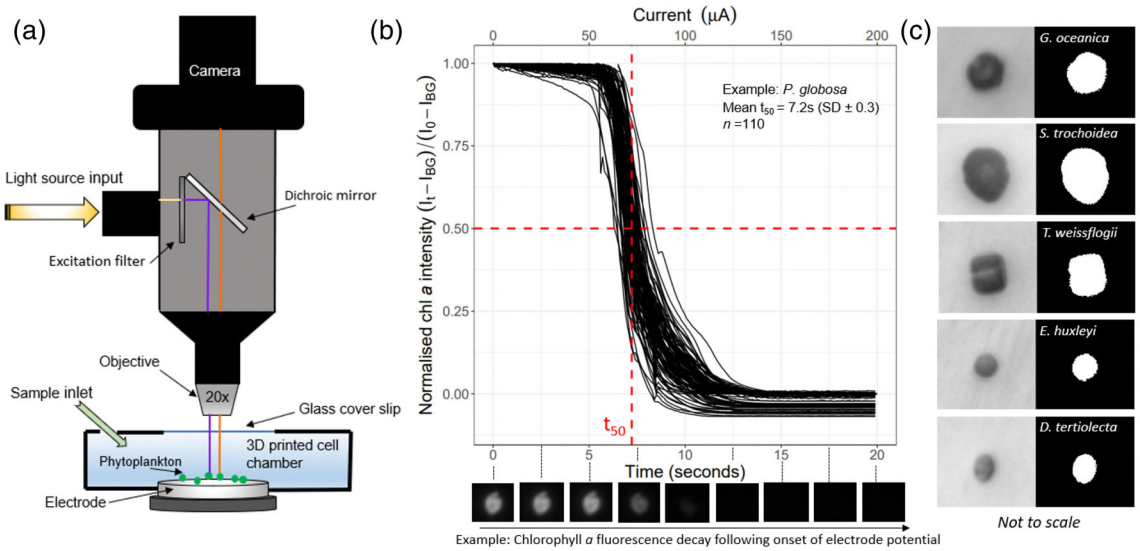

Fig. 1. (**a**) a simple schematic diagram of the electrochemistry—fluorescence microscope set up adapted from Yu et al. (2022); (**b**) an example of normalized Chl *a* fluorescence transient data for the species *Phaeocystis globosa*, following onset of the potential (at time 0 s) and with a current ramping of 10 μA s^{-1}. Each black line represents a single cell measurement ($n = 110$), and the dashed red markings highlight the time point, t_{50}, where normalized fluorescence values have been reduced by 50%. The time series of images below the plot illustrate the loss of fluorescence with time for one individual cell. (**c**) Examples of brightfield images taken before the electrochemical experiments for a selection of strains (left column), and the respective estimate of projected pixel area that was subsequently used to determine the effective radius of each cell (after assuming a circular shape).

for the "susceptibility library" section) was "drop cast" onto the surface of the working electrode. After ~ 1 min of allowing the cells to be deposited on the surface, excess solution was gently drawn-off using a tissue. Immediately following this, the 3D-printed cell chamber was filled up to maximum capacity with culture growth medium via the sample inlet. Once the chamber was at capacity a glass cover slip was put in place.
2. Using the fluorescence microscope (Axio Examiner, Carl Zeiss Ltd), we focused on a field of view whereby we had a high proportion of phytoplankton cells on the electrode surface (mean number per experiment = 23 ± 18 SD, across 212 unique experimental image series).
3. With the microscope set in bright-field mode, we took an image of the starting positioning of the cells. These images were later used to obtain an estimate of effective cell radius (*see* Fig. 1c).
4. Next, switching the microscope to fluorescence mode, the cells were excited using a 475 ± 35 nm excitation filter and emission signal passed through a dichroic mirror specific to wavelengths > 590 nm for Chl *a* fluorescence detection. Simultaneously, the galvanostatic control was synchronized with the camera and data acquisition was started. For the first 40 s of the electrochemical experiment, no potential was applied, allowing the fluorescence signal to stabilize. Following this, the current was ramped from 0 μA at a rate of 10 μA s^{-1} and images recorded at a capture rate of 10 fps. For each set of experiments the current was ramped until the chlorophyll signal had completely "switched off."
5. After the experiment, the 3D chamber was rinsed clean with deionized (DI) water and the above steps were repeated a minimum number of three times for each phytoplankton strain.

Following the experimental data collection, the raw fluorescence transient data were processed for each individual cell within each experimental time-series ($n = 4884$, across all strains) using ImageJ software (v1.53c, Fiji distribution), where "*n*" is the number of individual phytoplankton cell measurements. The integrated fluorescence intensity values for each individual cell (I_t) were corrected by subtracting the background signal of the electrode surface (I_{BG}) for all time points: $I_t - I_{BG}$, following this all values were then normalized by dividing by the fluorescence intensity at the onset of the potential (I_0): $(I_t - I_{BG})/(I_0 - I_{BG})$. We then used the normalized transient data to determine the time point for each individual cell where normalized intensity had decreased by 50% (t_{50}), *see* Fig. 1b. Due to the consistent linear ramping of current at 10 μA s^{-1} and that all phytoplankton cells imaged were settled on the surface of the electrode within the timescale of the experiments, we were able to determine the total charge required to be injected to reach t_{50} for each cell, and thus we herein refer to our Chl *a* susceptibility factor as charge at t_{50} (in mC). In some instances where there was significant movement of individual cells it was not possible to accurately measure the Chl *a* fluorescence profile throughout the time series, and subsequently data for these cells was considered erroneous and removed from the analysis.

For each cell specific Chl *a* fluorescence transient, we used the corresponding bright-field image collected prior to electrochemical experiments to derive a corresponding cellular area based on white pixel area of the cell (Fig. 1c). This was achieved by using the auto-threshold function in ImageJ freeware. From the total pixel area and using a predefined μm to pixel ratio (0.31 μm per pixel), we were able to estimate an effective radius (in μm) of each cell by assuming a circular 2D cell geometry (or a spherical cell). For cells in the picophytoplankton size range, due to the lack of contrast with the electrode surface it was not possible to accurately distinguish cell area, and therefore in these instances we obtained a measurement of mean cell pixel area by manually measuring the area of a subset of at least 10 cells per experimental time series (using ImageJ).

Assessment of the susceptibility library

With the two parameters of charge at t_{50} (mC) and effective radius (μm) defined for each individual cell, we assessed the applicability of the susceptibility library for distinguishing the cells into pre-defined groupings of relevance, as defined in the Culturing for the "susceptibility library" section. Prior to this assessment it was necessary to balance the dataset for even strain representation within each predefined grouping. This was necessary as there was limited control over the number of individual cell transients obtained per experimental image series per strain (due to unpredictable numbers of cells depositing on the electrode surface), resulting in under/over-representation within groups (*see* Supporting Information Table S3). To balance the data at the group level, we identified the strain within each group that had the lowest number of observations, and used that minimum number to randomly subset a sample of the same length for each of the other strains within the grouping level. This was achieved using the *sample_n* function in the R package *dplyr* (R version 4.2.2). The resultant balanced dataframe ($n = 2277$) was subsequently used to derive mean values at the group level and for the analyses described below (*see* Supporting Information Tables S4, S5 for balanced data).

First, looking at charge at t_{50} independently from radius, across all strains we see a large range spanning three orders of magnitude (*see* Supporting Information Table S4), from a mean of 0.08 mC (± 0.02 SD) for the pico-eukaryote *Ostreococcus tauri*, up to 7.34 mC (± 1.88 SD) for the dinoflagellate *Scripsiella trochoidea*. At the level of the predefined groupings described above we see the lowest mean charge at t_{50} within the "Picophytoplankton" of 0.11 mC (± 0.03 SD), and the greatest mean charge at t_{50} within the "Eustigmatales" 2.45 mC (± 0.41 SD), preceded by "Dinoflagellates" at 2.32 mC (± 2.22 SD; *see* Fig. 2b; Supporting Information

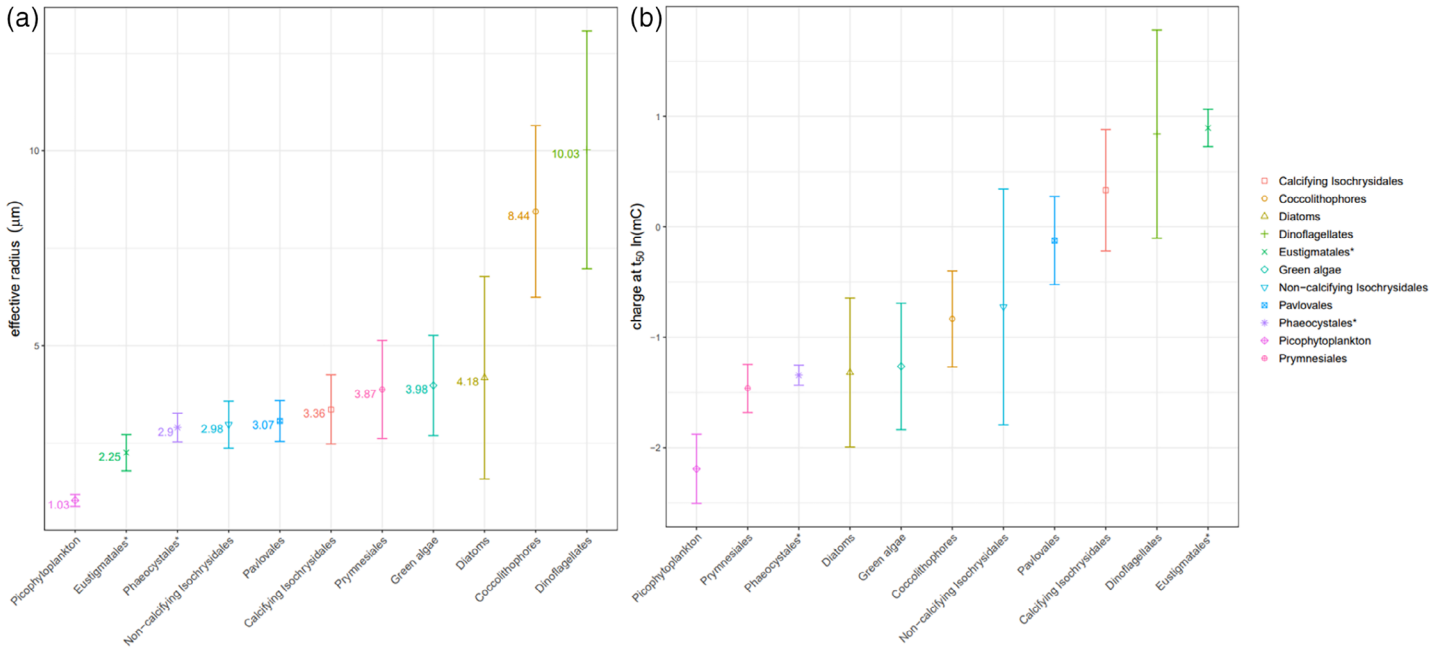

Fig. 2. (**a**) Mean effective radius (μm) at the level of each phytoplankton grouping defined in this study. The numbers alongside respective datapoints are the mean effective radius in μm. (**b**) Natural logarithm converted mean charge at t_{50} (mC) for each phytoplankton grouping. Data points represent the mean for each group, and error bars represent the standard deviation of the mean (*see* Supporting Information Table S5). Color coding and shapes represent each group (*see* legend). Note that the ordering on the *x*-axis is in ascending order for each plot, demonstrating that across the groups larger cell radius does not necessarily result in greater charge at t_{50}. Asterisk denotes groups that were just represented by a single species.

Table S5). The large range in these values indicate that there is a strong effect of cell grouping on the resilience to electrochemically driven oxidative stress. Critically, however, there is also considerable overlap in the values, as an example: "Calcifying Isochrysidales" have a mean charge at t_{50} of 1.39 mC ($\pm$ 0.57 SD), which sits well within the large deviation range of the "Dinoflagellates." Subsequently, in order to further distinguish the groupings in such instances, use of the effective radius can provide an additional dimension for separation where there is overlap. In the case of the previous example, we see that "Calcifying Isochrysidales" have a mean effective radius of 3.36 μm ($\pm$ 0.89 SD), whereas "Dinoflagellates" have a significantly larger mean effective radius of 10.03 μm ($\pm$ 3.05 SD; *see* Fig. 2a; Supporting Information Table S5). Taking this forward, we next use a random forest analysis to test the potential for single cell categorization across all the groups based on the variance in both charge at t_{50} and effective radius.

Random forest analysis uses the predefined classes (in this case the phytoplankton groupings) to construct a range of "decision trees" for discrimination of the individual observations (in this case each phytoplankton cell) based upon the predictor variables (in this case charge at t_{50} and effective radius) of a dataset. To effectively test the accuracy of classification, this requires input of a "training" dataset so that the random forest algorithm can create the necessary discrimination functions for the predefined classes. A "testing" dataset can then be used to determine the accuracy of the discrimination on an independent set of 'blind' observations. As an example of its application in a relevant field, random forest algorithms have previously been used to successfully distinguishing individual populations of phytoplankton strains from flow cytometry measurements on artificial communities (Bestion et al. 2020, 2021). While a flow cytometer records a wide range of fluorescence and light scattering variables per individual cell, here we are limited to testing the distinguishing power of our method with only the two aforementioned predictor variables (though additional variables for future iterations of the method are discussed later). Specifically, for our analysis, we used the "randomForest" function in the R package "randomForest"; this function uses Breiman's random forest algorithm for classification (Breiman 2001). From this we could determine categorization "decision trees" for two subsets of the susceptibility library data: (a) The key functional groups only (5 groups) with the balanced dataset (*see* Fig. 3) and (b) all groups (11 groups) with the balanced dataset (*see* Fig. 5; Supporting Information Table S5). For each subset, we randomly split the datasets using the *sample_n* function as described above, assigning 80% of data for the training component, and 20% for the testing. The two input predictor variables of charge at t_{50} and effective radius were natural log transformed prior to running the analysis. Following the training and subsequent testing, confusion matrices were returned to demonstrate the predictions of the random forest models (*see* Figs. 4, 6; Supporting Information Tables S6–S9). At the level of

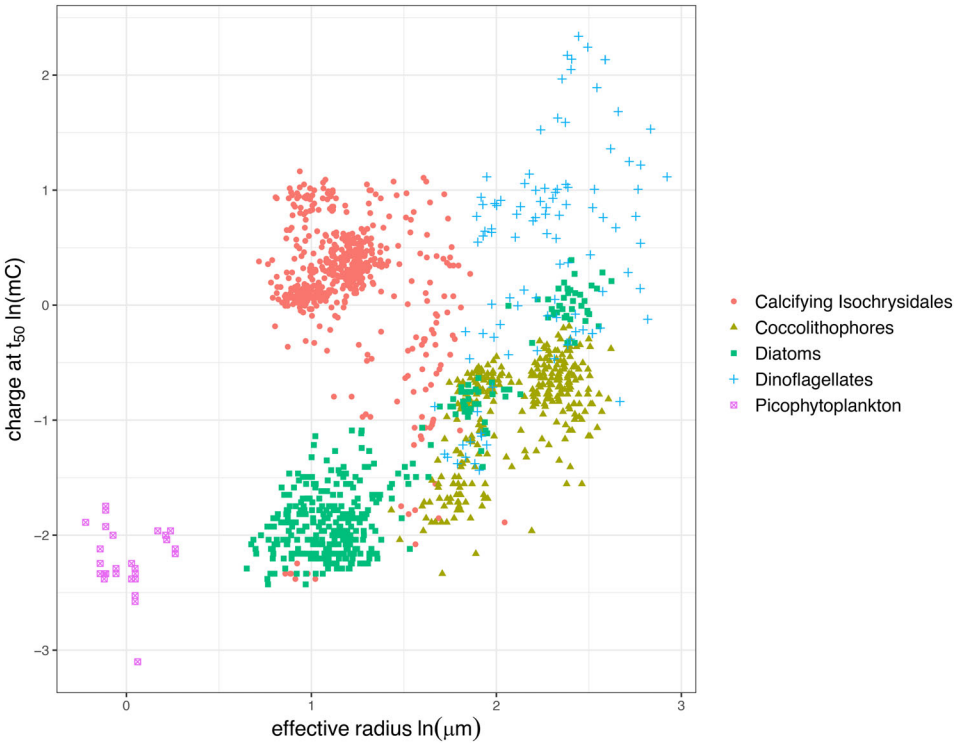

Fig. 3. A scatterplot of natural log charge at t_{50} (mC) against natural log effective cell radius (μm) for the "key functional groups" of cells measured in this study ($n = 1406$, *see* Supporting Information Table S5 for a summary of the balanced dataset). Although there is some overlap of the groupings, the random forest analysis on testing subset of this data returned an overall accuracy of 92% (*see* Fig. 4; Table 1; Supporting Information Table S7).

group for each testing subset, we investigated the prediction success in terms of recall, precision, and *F*1-score metrics (Kraft et al. 2022), *see* Tables 1 and 2.

Recall determines how well the random forest quantifies true positives (TP) for each class, that is, a higher recall means fewer false-negative predictions are made (FN):

$$\text{Recall} = \frac{\text{TP}}{\text{TP} + \text{FN}}$$

Precision determines how well incorrect false positives (FP) are rejected for each class, that is, a higher precision means fewer false positive predictions are made, and more true negatives (TN) are correctly identified:

$$\text{Precision} = \frac{\text{TP}}{\text{TP} + \text{FP}}$$

The *F*1-score combines both the recall and precision into a single metric to define the overall prediction accuracy for each class:

$$F1 - \text{score} = \frac{2 \times (\text{precision} \times \text{recall})}{\text{precision} + \text{recall}}$$

In addition to the above, overall accuracy of the random forest was returned to demonstrate the success rate of categorization across the testing dataset:

$$\text{Accuracy} = \frac{\text{TP} + \text{TN}}{\text{TP} + \text{FP} + \text{TN} + \text{FN}}$$

From training the random forest with the balanced dataset of the key groups only, we found there to be an overall testing accuracy of 92% (*see* Table 1; Supporting Information Table S7). The high level of accuracy is perhaps unsurprising considering the visual clustering of the datapoints (*see* Fig. 3). Within the groupings, however, some classifications perform better than others. "Picophytoplankton" are correctly classified in all instances (recall = 1), and this is primarily driven by their much smaller size relative to the other groups. "Calcifying Isochrysidales" are the next best predicted group with a recall of 0.99, and this appears to primarily be driven by their greater electrochemical resilience (i.e., greater charge at t_{50}) relative to cells of a similar small size. The poorest performance was in classifying "Dinoflagellates," with a recall of 0.71, albeit having a precision score of 0.81. This is likely due to considerable variation in the charge at t_{50} within this group, meaning that some strains of dinoflagellate are misclassified as larger diatoms and coccolithophore, contributing to a greater number of false negatives in this instance. On the whole, the fact that all five of the key groups had *F*1-scores > 0.75 is an indication that the electrochemical sensitivity provides a good degree of separation, in combination with size. Nonetheless, in order to be more reflective of the diversity of nanophytoplankton found in naturally

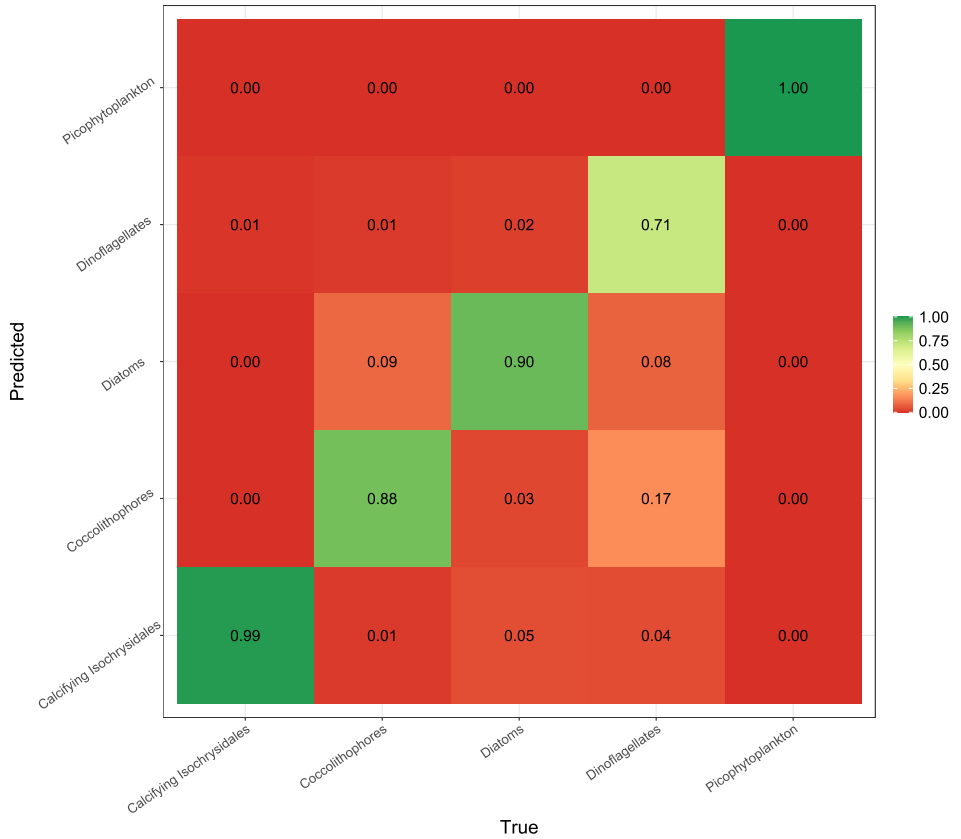

Fig. 4. A normalized confusion matrix demonstrating the prediction success of testing the random forest model with just the key groups included. To normalize, predicted number of cases were divided by the true total number of cases in each group (*see* Supporting Information Table S7 for original values).

Table 1. Evaluation metrics obtained from testing the random forest model trained for the key groups only.

Group	Recall	Precision	*F*1-score
Calcifying Isochrysidales	0.99	0.95	0.97
Coccolithophores	0.88	0.91	0.89
Diatoms	0.9	0.89	0.9
Dinoflagellates	0.71	0.81	0.76
Picophytoplankton	1	1	1
Overall accuracy			0.92

occurring communities, we next considered the level of performance once all of the other groups are included in the random forest analysis (*see* Figs. 5, 6).

When all the groupings are considered, following training, the overall accuracy on testing was 71% (*see* Table 2). The lower level of accuracy compared to the interpretation with only the key groups is also unsurprising, given that the number of potential classes in the random forest has more than doubled (5–11) and considering the greater extent of overlap in the group level clustering of the datapoints (*see* Fig. 5). Despite the overall reduction in accuracy, all the key groups maintain a relatively high level of predictability with all five returning recall, precision and *F*1-scores of more than 0.6. Of the key groups, the biggest reduction in performance is in the "Diatom" group, with recall being reduced from 0.9 in the key groups subset (*see* Table 1) to 0.63 when all groups are included. An element of confusion in this instance is being caused by cell types belonging to the other groups, such as "Non-calcifying Isochrysidales" and "Prymnesiales," which have similar size and electrochemical susceptibility distributions. Of the additional groups, the best performing were the "Pavlovales" with an *F*1-score of 0.68, closely followed by "Prymnesiales" and "Eustigmatales," both with *F*1-scores of 0.67. The worst performing were "Green algae" and "Non-calcifying Isochrysidales" with *F*1-scores of 0.33 and 0.39, respectively. In both cases, considerable confusion was coming from "Diatoms" and "Calcifying Isochrysidales," and specifically for "Green algae" there was substantial confusion with "Non-calcifying Isochrysidales." As dinoflagellates are often the group most commonly associated with harmful algal blooms, it is interesting to note that we see a higher precision (0.82) than recall (0.75) for this group. This indicates that while the random forest model is better at rejecting false positives, it could be improved in terms of reducing false

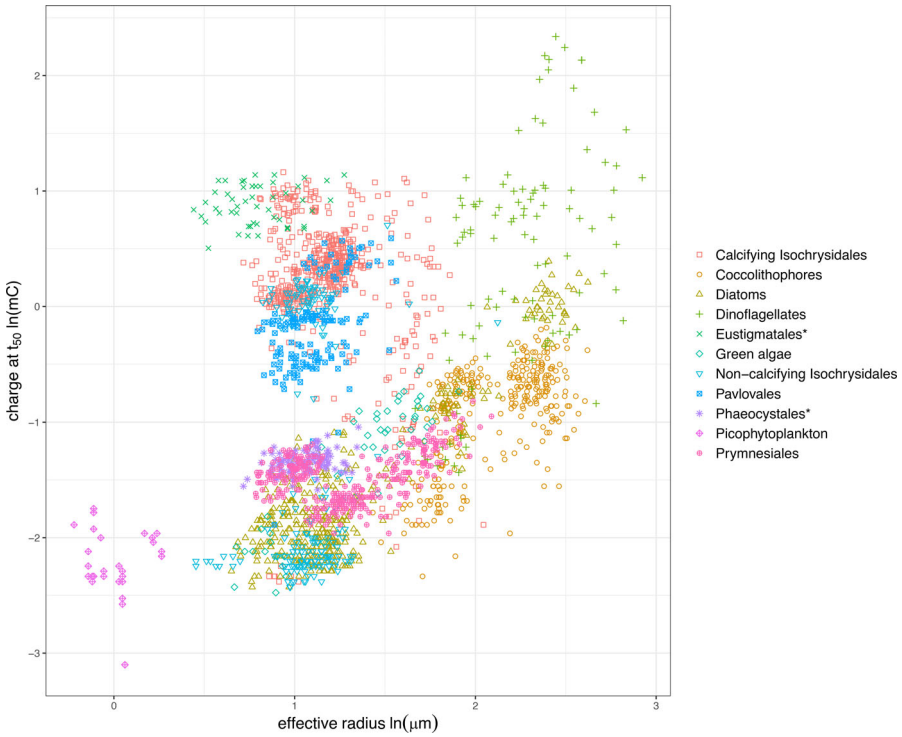

Fig. 5. A scatterplot of natural log charge at t_{50} (mC) against natural log effective cell radius (μm) for all groups of cells measured in this study ($n = 2277$, *see* Supporting Information Table S5 for a summary of the data presented here). Compared to Fig. 3, where just the key functional groups are presented, we now see more overlap of the groupings. The random forest analysis on the testing subset of this data returned an overall accuracy of 71% (*see* Fig. 6; Table 2; Supporting Information Table S9). Asterisk denotes groups that were just represented by a single species.

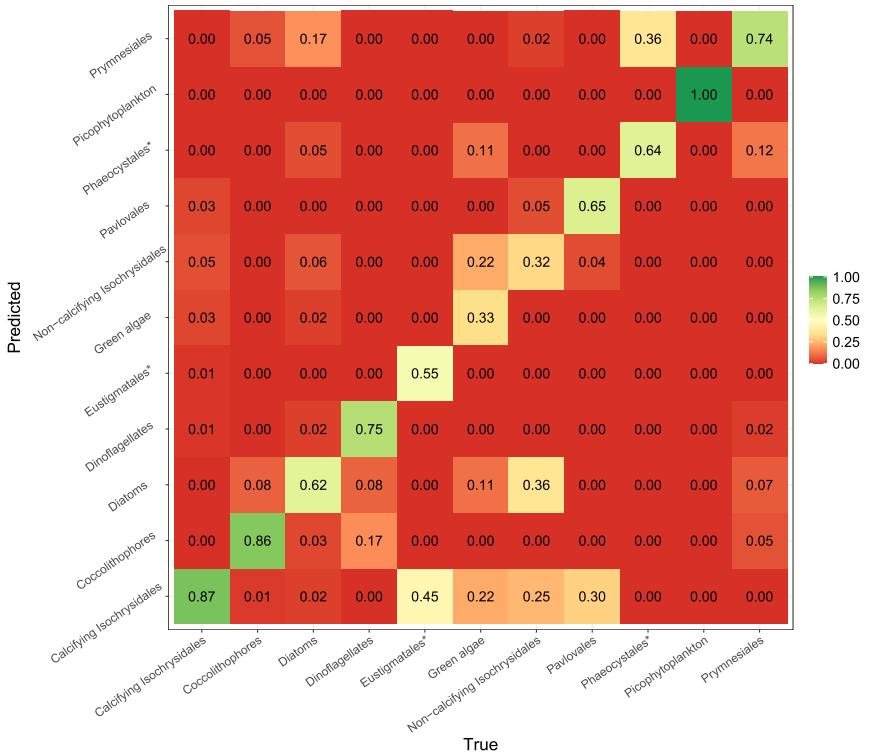

Fig. 6. A normalized confusion matrix demonstrating the prediction success of testing the random forest model with all groups included. To normalize, predicted number of cases were divided by the true total number of cases in each group (*see* Supporting Information Table S9 for original values). Asterisk denotes groups that were just represented by a single species.

Table 2. Evaluation metrics obtained from testing the random forest model trained for all groups.

Group	Recall	Precision	*F*1-score
Calcifying Isochrysidales	0.87	0.8	0.83
Coccolithophores	0.86	0.87	0.86
Diatoms	0.63	0.65	0.64
Dinoflagellates	0.75	0.82	0.78
Eustigmatales*	0.55	0.86	0.67
Green algae	0.33	0.33	0.33
Non-calcifying Isochrysidales	0.32	0.5	0.39
Pavlovales	0.65	0.71	0.68
Phaeocystales*	0.64	0.54	0.58
Picophytoplankton	1	1	1
Prymnesiales	0.74	0.61	0.67
Overall accuracy			0.71

*Groups that were just represented by a single species.

negatives (i.e., true cases of dinoflagellate that are being missed). From an applicability point of view, this could suggest that as things stand, improvement is needed if such a technique was to be employed to monitor for potentially harmful algae.

Significantly, of the key groups, there were some notable high performers following testing, despite the inclusion of the other groupings: "Calcifying Isochrysidales" with a recall of 0.87, "Coccolithophores" a recall of 0.86, and for "Picophytoplankton" recall remained at 1. In the case of the "Coccolithophores," their relatively strong predictability is likely due to their low electrochemical resilience relative to their large size, in contrast to "Dinoflagellates" of a comparable size which generally have a greater resilience. "Calcifying Isochrysidales" on the other hand are highly distinguishable for their remarkable electrochemical resilience relative to other groups of a similar smaller size. This poses some key questions about the underlying mechanism of this technique for distinguishing cell types across the groups: How much is cell size driving the electrochemical resilience? Are there any contradicting exceptions to any potential size scaling? With this in mind, we next scrutinize the effect of size on the susceptibility factor to see how much this is driving the overall resilience to the oxidative stress across the groups.

Understanding the mechanism: The size scaling of the relationship and size adjusted resilience

Using the balanced dataset of all groupings, we investigated if there was a significant linear relationship between natural log transformed charge at t_{50} and effective radius (*see* Fig. 7). This was achieved using the *lme4* package in R for linear mixed effects modeling, whereby we fitted and compared linear models to the data both with and without the random effect of grouping on both the intercept and slope of the

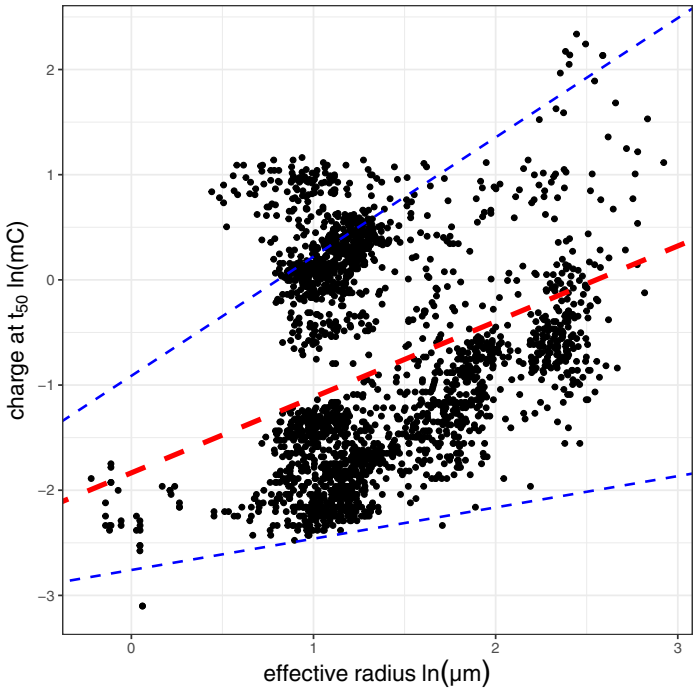

Fig. 7. A scatterplot of natural log charge at t_{50} (mC) against natural log effective cell radius (μm) of cells measured in this study, following the balancing of strain representation per group ($n = 2277$, *see* Supporting Information Table S4 for a summary of the data presented here). The red line indicates the overall slope (0.72) of the allometric relationship modeled using linear mixed effects with the random effect of grouping on the slope and intercept factored for, and the blue dashed lines indicate the 95% confidence of this model fit (slopes of 0.30 and 1.13 for lower and upper, respectively), *see* Supporting Information Tables S10 and S11 for statistics.

response. Of the two models, the model including the random effect of grouping on both the slope and intercept scored more favorably than the model without (*see* Supporting Information Table S10), indicating that there was an overall significant positive linear scaling between charge at t_{50} and effective radius ($p < 0.001$), but that this scaling was highly variable across the groupings. The overall model returned a slope value of 0.72 (95% CIs: 0.30–1.13). Out of the 11 "groups," 7 of them had significant positive within group size dependence, notably "Green algae," "Diatoms," and "Dinoflagellates" had particularly strong scaling of more than 1 (*see* Supporting Information Fig. S7; Table S11). There was no significant size scaling within the groups of "Picophytoplankton," and "Eustigmatales," "Phaeocystales"; this is perhaps unsurprising given that the latter two were only represented by one single strain. Notably, the only group that had a significant negative size scaling were the "Calcifying Isochrysidales," −0.48 (95% CIs: −0.66 to −0.31).

On the whole, this demonstrates that across most of the groupings there is an intrinsic allometric scaling of charge required to "switch-off" the Chl *a* signal. This was previously found at the species level in a recent study by Yu et al.

(2023), which demonstrated that differing electrochemical susceptibility of life stages of *Chlamydomonas concordia*, were primarily driven by size variation in the different cell types, and not necessarily an underlying biological factor (Yu et al. 2023). Consequently, we could postulate that any significant differences in electrochemical susceptibility following a size normalization might therefore indicate which of the groupings in this study have an 'unknown' underlying biological feature that results in higher or lower resilience. We investigated this by normalizing all charge at t_{50} values for size, by simply dividing charge (mC) by effective radius (μm) for each of the individual measurements in the balanced dataset (*see* Fig. 8).

Following size normalization of the charge at t_{50}, we carried out pairwise comparisons across the groups using Pairwise Wilcoxon Rank Sum testing (due to the non-parametric distribution of data in most of the groups), for this we used the function *pairwise.wilcox.test* in the R package *stats*, with *p.adjust.method* set to the "Bonferroni" correction of p values, see Supporting Information Table S12. We see no significant difference between a number of the key groupings, notably "Diatoms" and "Coccolithophores" ($p = 0.388$), and "Picophytoplankton" and "Dinoflagellates" ($p = 0.325$). Given that "Diatoms" in this dataset have a mean effective radius of 4.18 μm ($\pm$ 2.60 SD) and "Coccolithophores" of 8.44 μm ($\pm$ 2.20 SD), this indicates that most distinguishing between these two groups within the random forest must primarily be driven by size, given that their size normalized charge values are indistinguishable. Likewise, "Picophytoplankton" have a mean effective radius of 1.03 μm ($\pm$ 0.15 SD) and "Dinoflagellates" a mean effective radius of 10.03 μm ($\pm$ 3.05 SD), demonstrating extreme ends of the size spectrum within this dataset, yet after size normalization of their respective charge values they are indistinguishable in terms of their electrochemical resilience. Contrary to these observations, it is evident that there are some clear outliers, whereby following size normalization they are more distinguishable from the rest of the groups, notably "Calcifying Isochrysidales" and "Eustigmatales." In both cases, their size normalized charge was statistically greater than all the other groups, with "Eustigmatales" having the greatest overall per unit size resilience (*see* Fig. 8; Supporting Information Table S12). While we only have one strain representing "Eustigmatales" in this dataset, *Nannochloropsis granulata*, we might infer that there is something about the particular biology of these two groups that is driving their greater resistance to the high levels of oxidative stress. This is of relevance to the method, because across all our assessments using the random forest analysis it was the "Calcifying Isochrysidales" group that consistently retained one of the highest levels of prediction accuracy of the key functional groups. Taking our investigation further, we next take a closer look at within species variability to disentangle if any of the particular strains of *E. huxleyi* (from the "Calcifying Isochrysidales" group), representing different life stages and calcification morphologies (Green et al. 1996; Young et al. 2003; Bendif et al. 2023), can help to identify any further trends that may lead to understanding the biological mechanism.

Despite their differing coccosphere morphologies (ranging from light-, moderate-, and over-calcified features), in most cases across the four calcified (diploid) strains there was negligible difference in the size normalized charge at t_{50} (*see* Fig. 9; Supporting Information Table S13). This result is reassuring in terms of the proposed sensing technology, as it suggests that the within strain variance of "Calcifying Isochrysidales" is not too substantial to cause confusion with other groups. Of particular curiosity, the "1242" non-calcified diploid strain (RCC 1242) had a significantly greater charge per unit size relative to all other strains, and furthermore the "1217" non-calcified haploid strain (RCC 1217) was generally indistinguishable from the calcified strains (except for its calcified diploid version RCC 1216). This observation is of relevance to understanding any potential underlying mechanism to the sensor technology for two reasons. First, it indicates that there is minimal effect of the extracellular inorganic calcite layers in either increasing or reducing the resilience of the cell type. This is also more broadly demonstrated when comparing the "Calcifying Isochrysidales" group to the "Coccolithophores," the latter in many instances (e.g., *Coccolithus braarudii*) having much larger extracellular calcium carbonate shell volumes (Yang et al. 2022), yet relatively much faster "switch-off" times and lower size normalized charge tolerance under this method (*see* Fig. 2b; Supporting Information Fig. S9). Second, it suggests that there is something biologically different between the non-calcified and calcified diploid cells that is driving the discrepancy in the resilience. Disentangling this is beyond the scope of this study, but presents an avenue for further investigation as to why such cell types have greater resilience. Indeed, along a similar vein of thinking, exploring the biological differences of each of the groups against the highly resilient *Nannochloropsis granulata* could help to understand what is driving such resilience irrespective of the cell size. As a tentative suggestion, greater resilience could simply be determined by the membrane structure of the cell, whereby the presence of more membrane layers surrounding the cytoplasm and/or the plastids could potentially present a barrier acting to slow down the transmission of the oxidative radicals to the chlorophyll molecules (Yu et al. 2022). It has previously been reported that *Isochyrsidales* (and specifically *E. huxleyi* and *G. oceanica*) are distinctive from other coccolithophorids due to a number of different periplast and membrane features, including: unmineralized outer cell scales, more rigid double membrane structures of the peripheral endoplasmic reticulum, and unique long-chain membranous alkenones (Fujiwara et al. 2001). Perhaps it is features, such as these, slowing the transmission of radical oxidants to the chloroplasts of "Calcifying Isochrysidales," resulting in apparent resilience relative to other groups in this study.

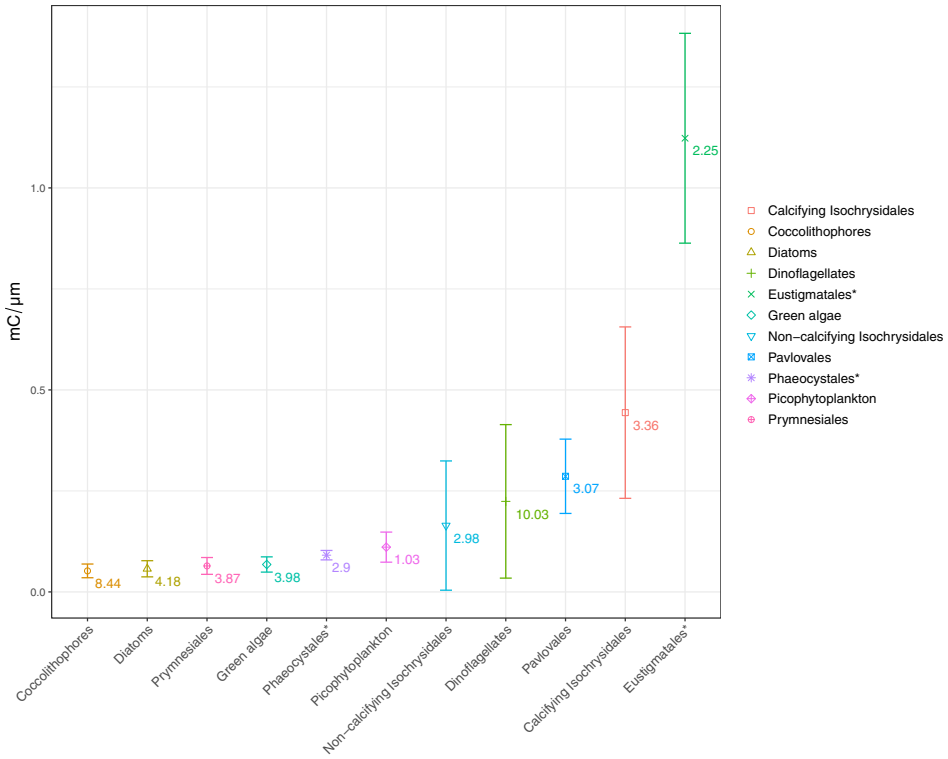

Fig. 8. Comparison of per group means of size normalized charge at t_{50}, following the balancing of strain representation per group. Data points represent the mean value for each group and the error bars are for standard deviation. The labeled numbers alongside the data points represent the mean effective radius for each of the groups (in μm), illustrating that in some instances there is a disproportionate resilience to the electrochemical charge relative to cell size—notably for "Calcifying Isochrysidales" and "Eustigmatales." For pairwise comparisons, see Supporting Information Table S12. Asterisk denotes groups that were just represented by a single species.

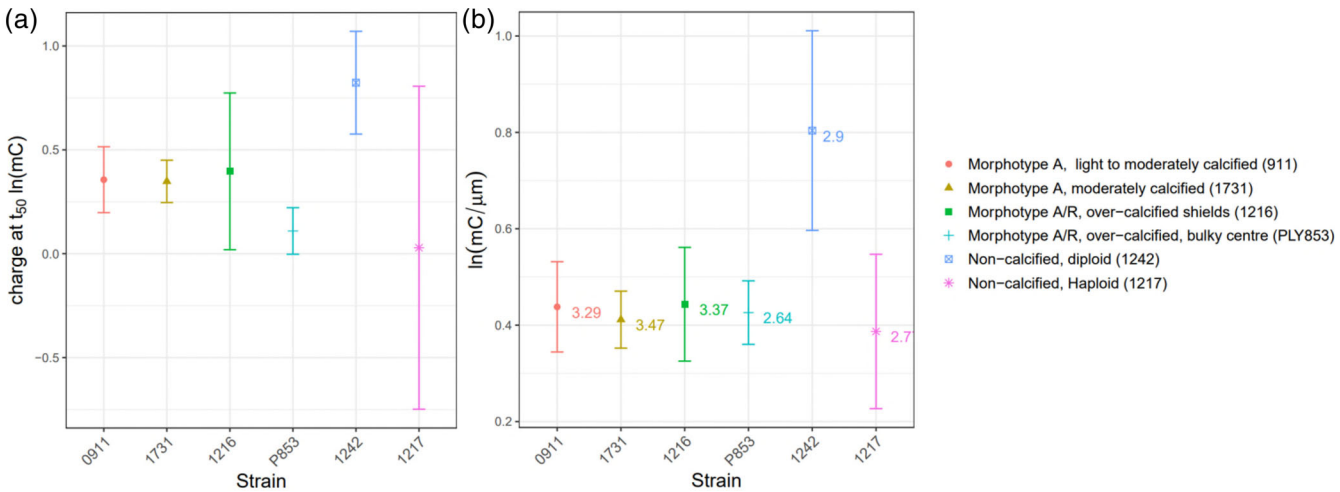

Fig. 9. (**a**) Comparison of natural log transformed mean charge at t_{50} across the different strains of *Emiliania huxleyi* representing different coccosphere morphologies (0911 [RCC911], 1731 [RCC1731], 1216 [RCC1216], [PLY853]), and non-calcified diploid and haploid life stages (1242 [RCC1242], (1217 [RCC1217]). For details on the strains, *see* Supporting Information Table S1. (**b**) Comparison of natural log transformed size normalized charge across the same strains. The labeled numbers alongside the data points represent the mean effective radius for each of the strains (in μm), illustrating that across the strains there is minimal difference in size. For pairwise comparisons, see Supporting Information Table S13. For both plots, data points represent the mean value for each group and the error bars are for standard deviation.

Discussion

Overall, our method has demonstrated a good degree of accuracy when it comes to making classifications of cell types into ecologically relevant groups. The groups that consistently had the greatest accuracy were "Calcifying Isochrysidales," "Coccolithophores," and "Picophytoplankton"; all of which maintained a recall of > 0.85, and precision and *F*1-scores of > 0.8, across the random forest predictions (both key group and all group libraries). The inclusion of the suspected "nano-phytoflagellate" groups did cause some overall reduction in the accuracy of the technique, from 92% to 71%, but given that we have just two variables to make predictions (charge at t_{50} and effective radius), this is something that we anticipate can be improved if the technique was adjusted to capture additional predictor variables. The findings of the susceptibility library assessment also demonstrate that following size normalization there must be some underlying biological feature that is enhancing the strong classification ability of some of the groups, notably "Calcifying Isochrysidales" and "Eustigmatales," and thus this presents an important avenue for further investigative studies into the potential mechanistic underpinnings.

Current applicability of the method and recommendations

Although we demonstrate the ability of our technique to classify nanophytoplankton into groups of relevance, it is critical that the method can quantify the abundance of different groups in natural seawater samples. This will require field testing alongside more traditional techniques, for example, microscope taxonomy and cytometry to validate the applicability of using a predefined susceptibility library based on a limited selection of 52 monocultures. Methodological and engineering advancements will need to be made to take this method to such a stage. As things stand, in obtaining the susceptibility measurements presented here, samples of an uncontrolled volume were drop cast following concentration by centrifugation and left to settle on the electrode beforehand (Kumar et al. 2020). Therefore, given the uncertainties around the volume of sample used, it was not possible to quantify the original abundance of cells in the samples measured. A prototype instrument that implements the fluoro-electrochemical technique with a flow-cell type system could help to overcome this issue, as both sample volume and flow rate could be quantifiable and controllable. To achieve the "current ramping" approach as demonstrated in this study it is likely that a series of in-flow ring electrodes with different applied currents, separated at periodic intervals, would be required in a future flow-type device. This may allow for a similar level of classification, but with the advantage of the high throughput of a flow-cell setup where number of events can be quantified per unit time, providing a measurement of actual abundance for the different classified cell types. Not only could this make the laboratory-based measurements higher throughput (akin to imaging flow cytometry), it would also be an essential step toward the long-term goal of the technique being used on autonomous platforms, whereby the collection of in situ spatiotemporal data of nanophytoplankton community structure would be invaluable to monitoring the effects of environmental change. From a practical point of view, our technique could lend itself well to long-term in situ monitoring via an autonomous platform. The electrochemical technique is reagent free (whereby seawater serves as the electrolyte), thus minimizing the need for regular retrieval of the device. Furthermore, the production of oxidants on the electrode surface provides an intrinsic anti-fouling mechanism; indeed, electrochemical generation of hydroxyl radicals is a technique that has been successfully used to rapidly kill invasive phytoplankton species in ship's ballast water within seconds, not dissimilar to what we see in the experiments presented here (Zhitao et al. 2005; Bai et al. 2010, 2012; Zhang et al. 2013). Given the relatively simple optics set-up of our technique, compared to others, it is also likely the key components be scaled down from the current lab set-up (*see* Fig.1a), making it more feasible for deployment in the field.

As mentioned previously, devices such as FlowCam, CytoSense, CytoBuoy, and IFCB use combinations of flow cytometry fluorescence measurements with rapid imaging of cells. While highly progressive in helping us to understand planktonic communities, they fall short in their ability to distinguish at the much smaller size ranges—especially when many cell types in the nanophytoplankton range can have a similar apparent morphology and size. Understandably, there is a consequent trade-off between magnification, image quality, and the size range of phytoplankton being measured. This is likely to make any machine learning algorithms poorer at the lower limits of the nanophytoplankton size range. The key novelty of our classifying technique at the nanophytoplankton level is the extra tool for distinguishing phytoplankton cell types that has not been previously applied: the electrochemical susceptibility of the Chl *a* fluorescence signal, which is less dependent on magnification and image resolution. We can get a good degree of categorization overall from simply combining the charge at t_{50} value with a simple effective radius estimate. We also demonstrate that our design has potential to distinguish picophytoplankton, as well as larger nanophytoplankton, spanning three orders of magnitude.

It was evident from our assessment that some groups were more easily predicted than others, especially when all the groups were considered. Of the key functional groups, our technique currently falls short when it comes to distinguishing diatoms (*F*1-score of 0.64, *see* Table 2), and of the other groups, the lowest accuracy was in predicting "Non-calcifying Isochrysidales" and "Green algae" (*F*1-scores of 0.39 and 0.33, respectively, *see* Table 2). Therefore, due to the differing levels of classification ability across the groups as things stand, it is likely the set-up would yield more promising in situ measurements from nanophytoplankton communities dominated by taxa belonging to the more easily classifiable groups presented here. To advance our method further, and with minimal increase in cost, a couple of

adjustments to both the apparatus and method could give us additional variables that will likely improve predictive ability. First, with the addition of more excitation and emission pathways, a measurement of secondary Chl *b* pigment fluorescence could be obtained. In marine phytoplankton, this pigment is unique to chlorophytes (or green algae). In the nanophytoplankton range, a large degree of confusion for our method was between the "Diatoms" and "Green algae," and therefore this addition would help to reduce this. Such an advancement could also assist at the picophytoplankton scale, where the majority of pico-eukaryotes are either prasinophytes containing Chl *b* or cyanobacteria containing phycocyanin (a chlorophyll accessory pigment, also with distinguishable autofluorescence properties).

Second, where there is overlap between calcified cell groups and others, we might be able to use the intrinsic dissolution of the calcite during the electrochemical experiments to observe changes in the apparent radius before and after the experiment. In brief, the electrochemical oxidation of water means that H^+ is generated in the vicinity of the electrode, decreasing the pH around the cells. Consequently, it has been observed that during the short time span of the experimental measurements presented here, the smaller extracellular calcite coccospheres (e.g., *E. huxleyi*) can be completely dissolved, such that a before and after measure of cell radius could indicate the calcification of a cell. Previous work has demonstrated that such a method can also be applied to estimate the mass of extra-cellular calcium carbonate of entire coccospheres (Fan et al. 2022; Yang et al. 2022), which is another relevant measurement for understanding marine biogeochemical cycles, notably the "rain ratio" (Hutchins 2011). Having an additional predictor variable of the ratio of cellular radius before and after the fluoro-electrochemical experiment would thereby provide an entirely affordable and achievable additional dimension for improved differentiation of calcified and non-calcified cell types in the random forest algorithms, as well as generating an estimate of cellular calcite which could be of great value to ocean biogeochemists.

Lastly, additional predictor variables can be gained by taking advantage of the full range of data that is harvested from the experiments presented here. In terms of the Chl *a* fluorescence measurement, we only use a single parameter derived from each transient profile: charge at t_{50}. If the full transient profiles were to be assessed then it is likely this could improve the predictive power of the susceptibility library. Indeed, the shape of the transients appear to be idiosyncratic at a group-specific level (*see* Supporting Information Fig. S2). With this in mind, by extracting the time (and thus charge) data for additional stages of normalized Chl *a* fluorescence intensity (e.g., at 75%, 25%, and 0%) we are more likely to capture the variation in the shape, or gradient, of the "switch-off" profile. Likewise, in terms of the bright-field imaging, we only make a relatively crude interpretation of the cell radius. There are other variables that can be characterized from the images, such as the minor and major axis lengths to determine aspect ratio (and thus giving an indication on how spherical or elongated a cell is).

Taking things forward, while we demonstrate relatively good accuracy with just using the two predictor variables used in this study (charge at t_{50} and effective radius), a greater wealth of data could be yielded with only minor methodological tweaks (as suggested above). By training the random forest with more variables (such as: secondary pigment fluorescence, change in cell radius before and after experiment, Chl *a* fluorescence at different stages in the "switch-off," and various cell characteristics from 2D bright-field images) this is likely to improve the classification accuracy across more of the relevant groups.

Overall, following on from the promising results presented here, we foresee that our technique (subject to the improvements discussed) could be extremely complimentary to broader efforts of ocean monitoring. The focus of our technique on the nanophytoplankton size fraction can add detail that is currently missing from existing techniques. As we demonstrate, there is potential for distinguishing cells into relevant groupings, going beyond the limited capacity of standard flow cytometry where, as things stand, only a select few of the functional groups can be differentiated within nanoeukaryotic communities; coccolithophores and cryptophytes (Tarran et al. 2006; Tarran and Bruun 2015). Furthermore, as discussed above, the application of our technique would help to unlock detail at the finer size scale that is also poorly characterized by current in situ imaging flow cytometry. Through developing our "susceptibility library" with a diverse range of taxa, we also expect that our technique could help to tease out more information from previously labeled unknown "nano-phytoflagellate" populations in natural communities, which are notoriously problematic for taxonomists due to their similar sizes and morphology when viewed under the microscope (Widdicombe et al. 2010; Piwosz 2019). For example, both "Pavlovales" and "Prymnesiales" haptophyte groups in this study had *F*1-scores of > 0.65, indicating that while they might be of a similar size and morphology (and thus are likely "nano-phytoflagellate" candidates), they are somewhat distinguishable by their susceptibility to the electrochemically driven oxidative conditions.

Summary

We have presented a novel fluoro-electrochemical technique for classifying marine nanophytoplankton, and critically assessed this by testing its ability to predict phytoplankton groupings from two simple parameters: charge required to reduce per cell Chl *a* fluorescence by 50% and effective cell radius. This returned an excellent degree of accuracy when only considering taxa belonging to key functional groups (5 groups), but a reduced degree of accuracy when a broader range of groups, encompassing likely "nano-phytoflagellates," were considered (11 groups). We demonstrate that the technique relies

on the general positive size scaling of the susceptibility across the groups to provide additional distinguishing power, and when size is normalized for there are some groups that demonstrate exceptional resilience to the highly oxidative conditions of our technique, notably "Calcifying Isochrysidales" and "Eustigmatales." This presents an avenue for further investigation into the biological underpinnings of this new method. Although the technique currently has its limitations as we report, with advancement of the set-up to make complimentary measurements, the predictive power of the method could be enhanced. Critically, if the technique is to eventually be used for real world in situ measurements, the next step of assessment is to test its ability in quantifying abundance of different groupings in natural samples alongside more traditional techniques. If such further testing yields positive results, we anticipate that our technique could be adapted to work in conjunction with autonomous platforms, with the potential to greatly enhance our ability in monitoring nanophytoplankton community structure.

References

Álvarez, E., M. Moyano, Á. López-Urrutia, E. Nogueira, and R. Scharek. 2014. Routine determination of plankton community composition and size structure: A comparison between FlowCAM and light microscopy. J. Plankton Res. **36**: 170–184. doi:10.1093/plankt/fbt069

Alves-De-Souza, C., T. S. Benevides, J. B. O. Santos, P. Von Dassow, L. Guillou, and M. Menezes. 2017. Does environmental heterogeneity explain temporal β diversity of small eukaryotic phytoplankton? Example from a tropical eutrophic coastal lagoon. J. Plankton Res. **39**: 698–714. doi:10.1093/plankt/fbx026

Anderson, S. I., A. D. Barton, S. Clayton, S. Dutkiewicz, and T. A. Rynearson. 2021. Marine phytoplankton functional types exhibit diverse responses to thermal change. Nat. Commun. **12**: 6413. doi:10.1038/s41467-021-26651-8

Anderson, T. R. 2005. Plankton functional type modelling: Running before we can walk? J. Plankton Res. **27**: 1073–1081. doi:10.1093/plankt/fbi076

Bai, M., Z. Zhang, X. Xue, X. Yang, L. Hua, and D. Fan. 2010. Killing effects of hydroxyl radical on algae and bacteria in Ship's ballast water and on their cell morphology. Plasma Chem. Plasma Process. **30**: 831–840. doi:10.1007/s11090-010-9252-5

Bai, M., Z. Zhang, N. Zhang, Y. Tian, C. Chen, and X. Meng. 2012. Treatment of 250 t/h ballast water in oceanic ships using ·OH radicals based on strong electric-field discharge. Plasma Chem. Plasma Process. **32**: 693–702. doi:10.1007/s11090-012-9369-9

Balzano, S., D. Marie, P. Gourvil, and D. Vaulot. 2012. Composition of the summer photosynthetic pico and nanoplankton communities in the Beaufort Sea assessed by T-RFLP and sequences of the 18S rRNA gene from flow cytometry sorted samples. ISME J. **6**: 1480–1498. doi:10.1038/ismej.2011.213

Barnes, M. K., G. H. Tilstone, D. J. Suggett, C. E. Widdicombe, J. Bruun, V. Martinez-Vicente, and T. J. Smyth. 2015. Temporal variability in total, micro- and nano-phytoplankton primary production at a coastal site in the Western English Channel. Prog. Oceanogr. **137**: 470–483. doi:10.1016/j.pocean.2015.04.017

Bendif, E. M., I. Probert, O. A. Archontikis, J. R. Young, L. Beaufort, R. E. Rickaby, and D. Filatov. 2023. Rapid diversification underlying the global dominance of a cosmopolitan phytoplankton. ISME J. **17**: 630–640. doi:10.1038/s41396-023-01365-5

Bestion, E., S. Barton, F. C. García, R. Warfield, and G. Yvon-Durocher. 2020. Abrupt declines in marine phytoplankton production driven by warming and biodiversity loss in a microcosm experiment. Ecol. Lett. **23**: 457–466. doi:10.1111/ele.13444

Bestion, E., B. Haegeman, S. Alvarez Codesal, A. Garreau, M. Huet, S. Barton, and J. M. Montoya. 2021. Phytoplankton biodiversity is more important for ecosystem functioning in highly variable thermal environments. Proc. Nat. Acad. Sci. U.S.A. **118**. doi:10.1073/pnas.2019591118

Bolaños, L. M., and others. 2020. Small phytoplankton dominate western North Atlantic biomass. ISME J. **14**: 1663–1674. doi:10.1038/s41396-020-0636-0

Breiman, L. 2001. Random forests. Mach. Learn. **45**: 5–32. doi:10.1023/A:1010933404324

Camoying, M. G., and A. T. Yñiguez. 2016. FlowCAM optimization: Attaining good quality images for higher taxonomic classification resolution of natural phytoplankton samples. Limnol. Oceanogr. Methods **14**: 305–314. doi:10.1002/lom3.10090

Chase, A. P., S. J. Kramer, N. Haëntjens, E. S. Boss, L. Karp-Boss, M. Edmondson, and J. R. Graff. 2020. Evaluation of diagnostic pigments to estimate phytoplankton size classes. Limnol. Oceanogr. Methods **18**: 570–584. doi:10.1002/lom3.10385

Collier, J. L. 2000. Flow cytometry and the single cell in phycology. J. Phycol. **36**: 628–644. doi:10.1046/j.1529-8817.2000.99215.x

de Vargas, C., and others. 2015. Eukaryotic plankton diversity in the sunlit ocean. Science **1979**: 348. doi:10.1126/science.1261605

Dubelaar, G. B. J., P. L. Gerritzen, A. E. R. Beeker, R. R. Jonker, and K. Tangen. 1999. Design and first results of CytoBuoy: A wireless flow cytometer for in situ analysis of marine and fresh waters. Cytometry **37**: 247–254. doi:10.1002/(SICI)1097-0320(19991201)37:4<247::AID-CYTO1>3.0.CO;2-9

Dugenne, M., M. Thyssen, D. Nerini, C. Mante, J. C. Poggiale, N. Garcia, F. Garcia, and G. J. Grégori. 2014. Consequence of a sudden wind event on the dynamics of a coastal phytoplankton community: An insight into specific population

growth rates using a single cell high frequency approach. Front. Microbiol. **5**. doi:10.3389/fmicb.2014.00485

Fan, X., C. Batchelor-McAuley, M. Yang, S. Barton, R. E. M. Rickaby, H. A. Bouman, and R. G. Compton. 2022. Quantifying the extent of calcification of a Coccolithophore using a coulter counter. Anal. Chem. **94**: 12664–12672. doi:10.1021/acs.analchem.2c01971

Finkel, Z. V., J. Beardall, K. J. Flynn, A. Quigg, T. A. V. Rees, and J. A. Raven. 2010. Phytoplankton in a changing world: Cell size and elemental stoichiometry. J. Plankton Res. **32**: 119–137. doi:10.1093/plankt/fbp098

Fragoso, G. M., A. J. Poulton, N. J. Pratt, G. Johnsen, and D. A. Purdie. 2019. Trait-based analysis of subpolar North Atlantic phytoplankton and plastidic ciliate communities using automated flow cytometer. Limnol. Oceanogr. **64**: 1763–1778. doi:10.1002/lno.11189

Fuchs, R., and others. 2022. Automatic recognition of flow cytometric phytoplankton functional groups using convolutional neural networks. Limnol. Oceanogr. Methods **20**: 387–399. doi:10.1002/lom3.10493

Fujiwara, S., M. Tsuzuki, M. Kawachi, and N. Minaka. 2001. Molecular phylogeny of the haptophyta based on the rbcL gene and sequence variation in the spacer region of the RUBISCO operon 1. J. Phycol. **37**: 121–129. doi:10.1046/j.1529-8817.2001.037001121.x

Green, J., P. Course, and G. Tarran. 1996. The life-cycle of *Emiliania huxleyi*: A brief review and a study of relative ploidy levels analysed by flow cytometry. J. Mar. Syst. **9**: 33–44. doi:10.1016/0924-7963(96)00014-0

Haraguchi, L., H. Jakobsen, N. Lundholm, and J. Carstensen. 2017. Monitoring natural phytoplankton communities: A comparison between traditional methods and pulse-shape recording flow cytometry. Aquat. Microb. Ecol. **80**: 77–92. doi:10.3354/ame01842

Hutchins, D. A. 2011. Forecasting the rain ratio. Nature **476**: 41–42. doi:10.1038/476041a

Irisson, J.-O., S.-D. Ayata, D. J. Lindsay, L. Karp-Boss, and L. Stemmann. 2022. Machine learning for the study of plankton and marine snow from images. Ann. Rev. Mar. Sci. **14**: 277–301. doi:10.1146/annurev-marine-041921

Kraft, K., and others. 2021. First application of IFCB high-frequency imaging-in-flow cytometry to investigate bloom-forming filamentous cyanobacteria in the Baltic Sea. Front. Mar. Sci. **8**. doi:10.3389/fmars.2021.594144

Kraft, K., and others. 2022. Towards operational phytoplankton recognition with automated high-throughput imaging, near-real-time data processing, and convolutional neural networks. Front. Mar. Sci. **9**. doi:10.3389/fmars.2022.867695

Kumar, A. K. S., Y. Zhang, D. Li, and R. G. Compton. 2020. A mini-review: How reliable is the drop casting technique? Electrochem. Commun. **121**: 106867. doi:10.1016/j.elecom.2020.106867

Leblanc, K., and others. 2018. Nanoplanktonic diatoms are globally overlooked but play a role in spring blooms and carbon export. Nat. Commun. **9**: 953. doi:10.1038/s41467-018-03376-9

Litchman, E., and C. A. Klausmeier. 2008. Trait-based community ecology of phytoplankton. Annu. Rev. Ecol. Evol. Syst. **39**: 615–639. doi:10.1146/annurev.ecolsys.39.110707.173549

Lombard, F., and others. 2019. Globally consistent quantitative observations of planktonic ecosystems. Front. Mar. Sci. **6**. doi:10.3389/fmars.2019.00196

López-Sandoval, D. C., T. Rodríguez-Ramos, P. Cermeño, C. Sobrino, and E. Marañón. 2014. Photosynthesis and respiration in marine phytoplankton: Relationship with cell size, taxonomic affiliation, and growth phase. J. Exp. Mar. Biol. Ecol. **457**: 151–159. doi:10.1016/j.jembe.2014.04.013

Marañón, E., P. Cermeño, D. C. López-Sandoval, T. Rodríguez-Ramos, C. Sobrino, M. Huete-Ortega, J. M. Blanco, and J. Rodríguez. 2013. Unimodal size scaling of phytoplankton growth and the size dependence of nutrient uptake and use. Ecol. Lett. **16**: 371–379. doi:10.1111/ele.12052

Morel, F. M. M., J. G. Rueter, D. M. Anderson, and R. R. L. Guillard. 1979. Aquil: A chemically defined phytoplankton culture medium for trace metal studies. J. Phycol. **15**: 135–141. doi:10.1111/j.1529-8817.1979.tb02976.x

Nair, A., S. Sathyendranath, T. Platt, J. Morales, V. Stuart, M. H. Forget, E. Devred, and H. Bouman. 2008. Remote sensing of phytoplankton functional types. Remote Sens. Environ. **112**: 3366–3375. doi:10.1016/j.rse.2008.01.021

Olson, R. J., and H. M. Sosik. 2007. A submersible imaging-in-flow instrument to analyze nano-and microplankton: Imaging FlowCytobot. Limnol. Oceanogr. Methods **5**: 195–203. doi:10.4319/lom.2007.5.195

Pinckney, J. L., C. R. Benitez-Nelson, R. C. Thunell, F. Muller-Karger, L. Lorenzoni, L. Troccoli, and R. Varela. 2015. Phytoplankton community structure and depth distribution changes in the Cariaco Basin between 1996 and 2010. Deep Sea Res. I Oceanogr. Res. Pap. **101**: 27–37. doi:10.1016/j.dsr.2015.03.004

Piwosz, K. 2019. Weekly dynamics of abundance and size structure of specific nanophytoplankton lineages in coastal waters (Baltic Sea). Limnol. Oceanogr. **64**: 2172–2186. doi:10.1002/lno.11177

Sieracki, C. K., M. E. Sieracki, and C. S. Yentsch. 1998. An imaging-in-flow system for automated analysis of marine microplankton. Mar. Ecol. Prog. Ser. **168**: 285–296. doi:10.3354/meps168285

Snoeijs, P., S. Busse, and M. Potapova. 2002. The importance of diatom cell size in community analysis. J. Phycol. **38**: 265–281. doi:10.1046/j.1529-8817.2002.01105.x

Sosik, H. M., and R. J. Olson. 2007. Automated taxonomic classification of phytoplankton sampled with imaging-in-flow cytometry. Limnol. Oceanogr. Methods **5**: 204–216. doi:10.4319/lom.2007.5.204

Stern, R., and others. 2023. Composition and patterns of taxa assemblages in the Western channel assessed by 18S

sequencing, microscopy and flow cytometry. J. Mar. Sci. Eng. **11**: 480. doi:10.3390/jmse11030480

Tarran, G. A., J. L. Heywood, and M. V. Zubkov. 2006. Latitudinal changes in the standing stocks of nano- and picoeukaryotic phytoplankton in the Atlantic Ocean. Deep Sea Res. II Top. Stud. Oceanogr. **53**: 1516–1529. doi:10.1016/j.dsr2.2006.05.004

Tarran, G. A., and J. T. Bruun. 2015. Nanoplankton and picoplankton in the Western English Channel: Abundance and seasonality from 2007–2013. Prog. Oceanogr. **137**: 446–455. doi:10.1016/j.pocean.2015.04.024

Ward, B. A., E. Marañón, B. Sauterey, J. Rault, and D. Claessen. 2017. The size dependence of phytoplankton growth rates: A trade-off between nutrient uptake and metabolism. Am. Nat. **189**: 170–177. doi:10.1086/689992

Widdicombe, C. E., D. Eloire, D. Harbour, R. P. Harris, and P. J. Somerfield. 2010. Long-term phytoplankton community dynamics in the Western English Channel. J. Plankton Res. **32**: 643–655. doi:10.1093/plankt/fbp127

Yang, M., C. Batchelor-Mcauley, L. Chen, Y. Guo, Q. Zhang, R. E. M. Rickaby, H. A. Bouman, and R. G. Compton. 2019. Fluoro-electrochemical microscopy reveals group specific differential susceptibility of phytoplankton towards oxidative damage. Chem. Sci. **10**: 7988–7993. doi:10.1039/c9sc02699a

Yang, M., C. Batchelor-McAuley, S. Barton, R. E. M. Rickaby, H. A. Bouman, and R. G. Compton. 2022. Single-entity coccolithophore electrochemistry shows size is no guide to the degree of calcification. Environ. Sci. Adv. **1**: 156–163. doi:10.1039/d2va00025c

Young, J., M. Geisen, L. Cros, A. Kleijne, C. Sprengel, I. Probert, and J. Østergaard. 2003. A guide to extant coccolithophore taxonomy. J. Nannoplankton Res. **1**: 1–132.

Yu, J., M. Yang, C. Batchelor-McAuley, S. Barton, R. E. M. Rickaby, H. A. Bouman, and R. G. Compton. 2022. Rapid Opto-electrochemical differentiation of marine phytoplankton. ACS Meas. Sci. Au **2**: 342–350. doi:10.1021/acsmeasuresciau.2c00017

Yu, J., M. Yang, C. Batchelor-McAuley, S. Barton, R. E. M. Rickaby, H. A. Bouman, and R. G. Compton. 2023. Does the life cycle stage matter for distinguishing phytoplankton via fluoro-electrochemical microscopy? Cell Rep. Phys. Sci. **4**: 101223. doi:10.1016/j.xcrp.2022.101223

Zhang, Y., M. Bai, C. Chen, X. Meng, Y. Tian, N. Zhang, and Z. Yu. 2013. ·OH treatment for killing of harmful organisms in Ship's ballast water with medium salinity based on strong ionization discharge. Plasma Chem. Plasma Process. **33**: 751–763. doi:10.1007/s11090-013-9464-6

Zhitao, Z., B. Mindong, Y. Bo, B. Mindi, and B. Xiyao. 2005. Treatment of invasive marine species on board by using micro-gap discharge plasma. Plasma Sci. Technol. **7**: 3025–3029. doi:10.1088/1009-0630/7/5/011

Acknowledgment

This research was conducted with the support from the Oxford Martin School Programme on Monitoring Ocean Ecosystems.

Conflict of Interest

None declared.

Submitted 29 March 2023
Revised 03 August 2023
Accepted 17 August 2023

Associate editor: Krista Longnecker